

Fast Spiral Coronary Artery Imaging

CRAIG H. MEYER,* BOB S. HU,† DWIGHT G. NISHIMURA,
AND ALBERT MACOVSKI‡

*Department of Electrical Engineering, Stanford University; †Division of Cardiovascular Medicine,
Stanford University Hospital; and ‡Departments of Electrical Engineering and Radiology,
Stanford University, Stanford, California 94305*

Received March 11, 1992; revised April 15, 1992; accepted April 15, 1992

A flow-independent method for imaging the coronary arteries within a breath-hold on a standard whole-body MR imager was developed. The technique is based on interleaved spiral k-space scanning and forms a cardiac-gated image in 20 heartbeats. The spiral readouts have good flow properties and generate minimal flow artifacts. The oblique slices are positioned so that the arteries are in the plane and so that the chamber blood does not obscure the arteries. Fat suppression by a spectral-spatial pulse improves the visualization of the arteries. © 1992 Academic Press, Inc.

INTRODUCTION

Coronary artery disease remains the major cause of mortality and morbidity in the industrialized world despite significant advances in its prevention. Reliable MR imaging of the coronary arteries could very well make significant contributions to the noninvasive diagnosis or monitoring of coronary artery disease. While it is premature to suggest that MR could supplant x-ray angiography with selective contrast injection, it is possible that MR coronary artery imaging could be used as a diagnostic adjunct, perhaps to monitor patients for re-stenosis after percutaneous transluminal angioplasty.

We have developed a flow-independent method for reliably imaging coronary arteries within a breath-hold using interleaved spiral k-space scanning. Other researchers have recently made significant progress in imaging the coronary arteries by other methods, including fast selective inversion recovery (1), oblique 2D “white-blood” gradient-echo methods (2, 3), sequential 2D white-blood gradient-echo methods (4, 5), 3D white-blood gradient-echo methods (6), oblique 2D “black-blood” spin-echo methods (7, 8), and multisection 2D black-blood spin-echo methods with subsequent reformatting (9). Our approach to imaging the coronary arteries grew out of our work in interleaved fast spiral imaging over the past few years (10–13), and in particular out of a project to produce a 3D heart movie from a series of 2D breath-held spiral heart movies (14). In that project, the coronary arteries were easily seen in the 2D images, but difficult to see in the projections through the entire 3D data set. This paper describes our efforts to adapt the sequence specifically to imaging the coronary arteries. This is also the first detailed description of our interleaved spiral scan sequence.

1992 SMRM Young Investigator’s Award Finalist.

* To whom correspondence should be addressed at 120 Durand, Information Systems Laboratory, Stanford University, Stanford, CA 94305.

There are a number of problems associated with coronary artery imaging, including cardiac motion, respiratory motion, and the neighboring presence of blood in the heart chambers and of static tissue, particularly fat, surrounding the vessels. We freeze the cardiac motion by gating, by reading out when the heart is relatively quiescent, and by using a relatively short readout window (17.5 ms). We freeze respiratory motion by completing the scan during a breath-hold (20 heartbeats or less). Because the coronary arteries lie along the surface of the heart, we are able to avoid the interference of blood in the chambers by carefully positioning the axial and graphically prescribed oblique slices so that the chamber blood does not obscure the vessels of interest. We suppress fat by using a spectral-spatial excitation pulse (15). Because most of the coronary tree lies in a bed of fat, this suppression provides excellent definition of the vessel wall.

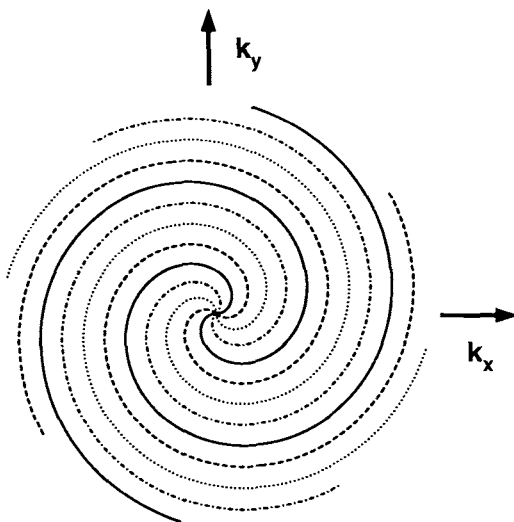
In this paper we first discuss the basic interleaved spiral imaging technique and some of its properties. We then discuss how it is applied to coronary artery imaging. We show the results obtained on some normal volunteers and one patient with known coronary artery disease and discuss these results.

METHODS

Spiral k -space trajectories were perhaps first mentioned as an alternative to Mansfield's original echo-planar trajectory (16) by Likes (17). Ljunggren (18) independently mentioned spiral trajectories and pointed out that a spiral trajectory would lead to an isotropic impulse response in the presence of T_2 decay during the scan, as compared to echo planar's anisotropic impulse response. Ahn *et al.* (19) published the first spiral images. They used a sequence that traced a constant-angular-velocity spiral and reconstructed the images using a convolution-backprojection algorithm. We showed that a constant-linear-velocity spiral is optimal from an SNR standpoint (10). Our spiral experiments have tried to approach this ideal of constant linear velocity in k space, subject to gradient risetime constraints (10, 13). We also studied square-spiral imaging, which has the advantage of requiring only one-dimensional interpolation and an FFT for reconstruction (10-13).

A spiral k -space trajectory can in theory be traversed in a single-shot mode, similar to the way echo-planar trajectories have been successfully employed (16, 20-22). We have concentrated our studies on interleaved spiral trajectories, however. A set of interleaved spiral k -space trajectories is shown in Fig. 1. The principal advantage of interleaving is practical: to traverse N interleaved spirals after N excitations, the required gradient power drops by about $1/N^2$, the required data collection bandwidth drops by $1/N$, and the SNR goes up by \sqrt{N} , compared to a single-shot scan. Interleaving has allowed us to perform all of our experiments on a standard commercial whole-body scanner, while still forming cardiac-gated images within a breath-hold. The gradient-power advantage of interleaving is also important in light of recent studies that have shown that strong echo-planar gradients can induce physiological effects (23, 24).

Interleaved spiral imaging appears to be well-suited to coronary artery imaging. It can produce a cardiac-gated image within a breath-hold on a commercial imager, which appears to be necessary for reliably seeing the coronary arteries (1, 3). The total readout period per heartbeat is shorter than alternatives that scan multiple 2DFT

FIG. 1. Interleaved spiral k -space trajectories.

lines with multiple excitations (1, 3); a readout typically takes less than 20 ms. It can be used with 90° excitations for high SNR and maximum wash-in in single-slice or multislice mode. Alternatively, it can be used in movie mode to provide temporal resolution and possibly some suppression of static tissue. Finally, spiral readouts have good flow properties.

The interleaved spiral sequence used for this work is shown in Fig. 2. It consists of a 15.5-ms spectral-spatial excitation pulse and 17.5-ms spiral readout gradients, followed by transverse gradients to return to the origin in k space and a spoiler gradient along the z axis. The spectral-spatial pulse suppresses fat while simultaneously selecting a slice; the spatial profile is Gaussian and the spectral profile is minimum-phase to minimize spectral dephasing during the pulse (25). The readout gradients are designed to image a 20-cm FOV in 20 interleaves. The gradients shown correspond to one of the interleaves; the other interleaves are traced by rotating the readout gradients using a hardware matrix multiplier on the GE Signa 1.5-T imager. Details about various aspects of this sequence are in the following sections.

SPIRAL GRADIENT GENERATION

The radius at any point on an Archimedean spiral is proportional to the cumulative angle traced out to that point. A spiral k -space trajectory is thus given by

$$\mathbf{k}(t) = A\tau(t)e^{i\omega\tau(t)}, \quad [1]$$

where $\tau(t)$ is some function of time. Setting $\tau(t) = t$ leads to the constant-angular-velocity spiral of Ahn *et al.* (19), with $\mathbf{g}(t) = iA\omega t e^{i\omega t} \approx d\mathbf{k}/dt$. A constant-angular-velocity spiral is undesirable from an SNR standpoint, because more time is spent near the center of k space than near the edge. One must weight the data unequally in the reconstruction, which leads to suboptimal SNR, assuming that the readout time

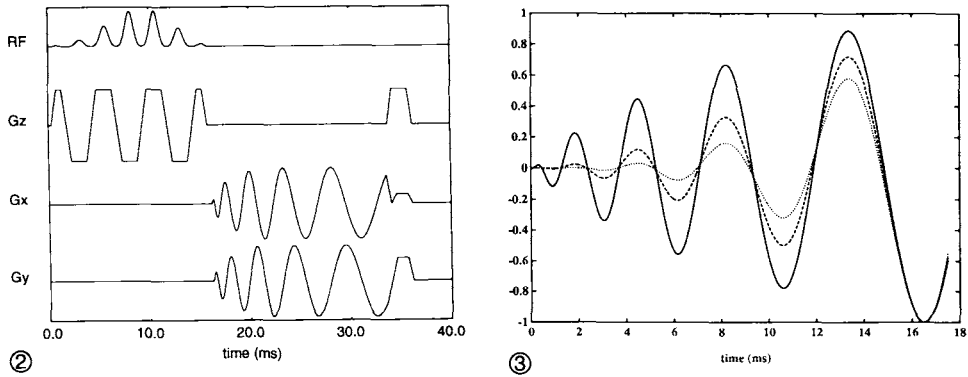


FIG. 2. Fast interleaved spiral pulse sequence. There is a spectral-spatial pulse for fat suppression followed by spiral readout gradients. The sequence is designed to image a 20-cm FOV in 20 excitations, with a resolution of 1.08 mm by 1.08 mm (186×186 pixels). The readout gradients corresponding to one interleaf are shown; the other interleaves are generated by rotating the gradients with a hardware rotation board.

FIG. 3. The first three moments of G_x of Fig. 2. Each moment is normalized to have the same maximum magnitude on the plot. The solid line is the zeroth moment (or k_x), the dashed line is the first moment, and the dotted line is the second moment. Note that all three moments return to near zero each time k_x returns to zero, which means that the gradients are relatively insensitive to motion during the scan.

is held constant and that one does not use any a priori knowledge about the image. If one is trying to complete the scan as quickly as possible, then a constant-angular-velocity spiral is also undesirable, because the readout gradients only reach their maximum amplitude at the end of the scan. Setting $\tau(t) = \sqrt{t}$ leads to a constant-linear-velocity spiral (ignoring the singularity at the origin), with $\mathbf{g}(t) = i\frac{1}{2} A\omega e^{i\omega\sqrt{t}}$. Since $\mathbf{g}(t)$ is proportional to the \mathbf{k} -space velocity, it is evident from this equation that the magnitude of the \mathbf{k} -space velocity is constant. The \sqrt{t} term appears in the equation for $\mathbf{k}(t)$, but not for $\mathbf{g}(t)$. Unfortunately, this gradient waveform is impossible to generate on a scanner, because it starts at full amplitude, and gradient subsystems have risetime constraints.

So we see that we want to choose $\tau(t) = \sqrt{t}$, except where such a choice violates gradient risetime constraints. The resulting gradient will be risetime-limited during the first part of the scan and then will be constant-amplitude for the rest of the scan. The problem of generating a risetime-limited spiral has been studied in the context of 2D selective excitation (26, 27), and we have adapted these algorithms to generate spirals under both risetime and amplitude constraints. The gradients in Fig. 2 were designed using this algorithm; they are risetime-limited for the first 5 ms of the scan and amplitude-limited for the remaining 12.5 ms. For a given FOV, increasing the number of interleaves allows the gradients to reach a given amplitude faster. Also, for a given number of interleaves, decreasing the imaged FOV has a similar effect. Each of these effectively reduces ω in Eq. [1]. Note that the complex magnitude of the gradients is constrained to meet the risetime and amplitude constraints, so that these constraints are not violated when the gradients are rotated during interleaving. For a noninterleaved spiral, some time savings can be achieved by optimizing the x and y gradients separately.

FLOW PROPERTIES

Experimentally we have observed that spiral gradients are relatively insensitive to flow-related dropouts and ghosting, even though the readouts are relatively long. A full study of this subject is beyond the scope of this paper, but here we will mention a few reasons that spirals have good flow properties. (By comparison, echo-planar gradients that collect all of \mathbf{k} space are known to be susceptible to flow-related dropouts and artifacts (28, 29).)

The most important flow-related advantage that spirals have is simply that the trajectory starts at the origin in \mathbf{k} space and moves out. This means that the center of \mathbf{k} space is collected at the start of the scan and thus with zero transverse moments of all orders. This factor alone reduces flow-related dropouts and ghosting due to phase variations from pulsatile flow. (The spectral-spatial excitation pulse of the sequence in Fig. 2 also has relatively good flow properties, reducing dephasing in the z direction.) Collecting the center of \mathbf{k} space first also keeps the echo time as short as possible, reducing spectral dropouts. Lastly, it means that spiral readouts do not suffer from the oblique flow artifact that 2DFT sequences suffer from (30).

Another advantage of spiral gradients is that the moments of all orders in a particular direction periodically return to zero together, further reducing flow-related dropouts. The expression for the n th complex moment of a constant-linear-velocity spiral is

$$M_n(t) = i \frac{1}{2} A \omega \int_0^t \tau^n e^{i\omega\sqrt{\tau}} d\tau \quad [2]$$

$$= A e^{i\omega\sqrt{t}} \sum_{j=0}^{2n+1} \left[(-1)^j \frac{(2n+1)!}{(2n+1-j)!} \frac{t^{1/2(2n+1-j)}}{(i\omega)^j} \right] + A \frac{(2n+1)!}{(i\omega)^{2n+1}}, \quad [3]$$

where $\mathbf{g}(t) = i \frac{1}{2} A \omega e^{i\omega\sqrt{t}}$. It can be seen from this equation that the moments of all orders oscillate together. This is true for any direction; for example, the real part of this expression gives the x -axis moment for the given gradient. The zero-crossing points are not quite identical early in the scan, but the absolute moment excursions are small then. The zero-crossing points actually get closer together later in the scan, becoming exactly coincident as $t \rightarrow \infty$. The general behavior of the moments for our optimized gradients is similar. Figure 3 shows the first three x -axis moments of the gradients of Fig. 2. These moments go to zero at approximately the same time.

There is another property of spirals that may be an advantage. Coherent "phase-encoding" ghosts do not appear when there are amplitude or phase variations from excitation to excitation, because the interleaving pattern is spiral instead of rectilinear. In this case energy is still displaced in the image, but the resulting spiral patterns tend to be less objectionable than a ghost image of a vessel would be. Also, because the center of \mathbf{k} space is collected after each excitation, the possibility of correcting for amplitude and phase variations exists; our initial experiments in this area have been inconclusive.

RECONSTRUCTION ALGORITHM

Reconstructing spiral images is of course more complicated than reconstructing 2DFT images; the collected data points do not in general fall on a 2D grid and so

some operations must be performed in addition to an FFT. We give a brief discussion of our reconstruction algorithm here, although the full details will be described in another paper. We use a gridding algorithm related to algorithms first used in radioastronomy (31–33). The basic idea of the algorithm follows.

1. Determine the receiver offset frequency, Δf . One method for doing this is to collect an FID with no readout gradients and to determine the peak of the spectrum of this FID. When using a surface coil, this method has the disadvantage of tending to focus on the chest wall instead of the heart. To counteract this, we try to determine the resonant frequency in the region of the image that is of the greatest interest. Currently this is done by reconstructing a single point of a low-resolution frequency map. This frequency information is obtained by a phase-difference procedure using data from two single-shot spiral scans collected at different TEs at the beginning of the scan.

2. Multiply the data points by $e^{i2\pi\Delta ft}$ to demodulate at the offset frequency determined in step 1.

3. Multiply the data points by $|\mathbf{g}(t)| \cdot |\sin[\arg\{\mathbf{g}(t)\} - \arg\{\mathbf{k}(t)\}]|$ to compensate for the varying density of the data points in \mathbf{k} space. The first term in this equation compensates for the varying \mathbf{k} -space velocity and the second term compensates for the increased density of the spirals near the origin.

4. Convolve the data into the 2D array. This is done by multiplying each density-compensated data point by a Kaiser–Bessel window a few grid points in width, evaluating the result at each grid point within the window, and adding the result into the array. An auxiliary array is used to keep track of the amount of energy put into each grid point, which is the product of the density-compensation factor and the Kaiser–Bessel function evaluation.

5. Normalize the energy in each grid point by dividing by the auxiliary array. If the density compensation of step 3 is done properly, this step results in only a minor correction.

6. Perform a complex 2D FFT.

7. Divide by the transform of the Kaiser–Bessel window to remove the apodization resulting from the convolution of step 4.

8. Take the magnitude of the result.

The reconstruction time for a 256×256 image for the 20-interleave sequence is under 16 s on a Sun IPX workstation. Although the reconstruction is done on an off-line computer, the entire process of data transfer and reconstruction is automatic, so that the image appears on the scanner's console as in normal operation.

OFF-RESONANCE CONSIDERATIONS

One of the disadvantages of spiral imaging is that the impulse response off-resonance is broadened, instead of just shifted as in 2DFT imaging (12, 34). Also, spiral readout times are typically longer than 2DFT readout times, which allows more time for phase accrual. Because of these factors, it is necessary to take steps to minimize the off-resonance artifacts. The steps include the following: (1) suppressing fat, because fat

and water will not simultaneously be in focus at 1.5 T; (2) designing the gradients to reach maximum gradient amplitude as quickly as possible; (3) using as many interleaves as possible for the application, because the blurring is related to the time it takes to reach a particular radius in k space; and (4) reconstructing at the proper frequency for the region of interest. It is also possible to de-blur spiral images in postprocessing, both with and without a phase map (34, 35).

The fat suppression in our sequence is provided by a spectral-spatial excitation pulse, a pulse with an oscillating gradient that is simultaneously selective in space and frequency (15). The overall envelope of the pulse provides the spectral selectivity and the subpulses provide the spatial selectivity. In order to achieve the thin spatial slices needed for this application, the slice-selection gradient of this pulse is oscillated at the relatively low frequency of 200 Hz, which is near the water-fat difference frequency at 1.5 T. Fat falls on a spectral sidelobe that has odd z symmetry (15), so that the fat signal is small when integrated over the slice. (The pulses described in Ref. (15) used a higher-frequency gradient, so that fat fell between spectral sidelobes.) The fat suppression of a spectral-spatial pulse is insensitive to variations in RF amplitude, unlike fat presaturation.

CORONARY ARTERY CONSIDERATIONS

The principal consideration in applying the sequence of Fig. 2 to coronary artery imaging is the proper positioning of the slice. While axial images of the heart made with this sequence reliably show the coronary arteries in cross section, it is usually necessary to use oblique slices to show large segments of the vessels in the plane. A typical localization sequence to image the left anterior descending coronary artery (LAD) is as follows: (1) Acquire one or more multislice axial spiral image sets to locate the left main coronary artery and the proximal LAD. (2) From these axial images, graphically prescribe a slice from the aortic root along the left main coronary artery. This results in a right-anterior-oblique (RAO) view of the LAD, a common angiographic view. It is usually possible to see the proximal circumflex artery and the posterior descending artery (PDA) in this view, as well as the left main coronary artery and the LAD. (3) From the RAO view, prescribe an oblique axial, or Grüntzig, view along the LAD. The resulting view shows the LAD and its diagonal branches. A similar procedure can be used to image the right coronary artery (RCA) in various views. Because each of the scans is completed in a breath-hold, the localization procedure can be completed rapidly.

The slice width is chosen to avoid significant interference from chamber blood or myocardium. Typically, the arteries are most visible when the slice width is between 3 and 10 mm. For some views, it is necessary to acquire several overlapping slices to view the entire vessel. Fortunately, the RCA, the LAD, and several other vessels lie in a bed of fat, so the fat suppression provided by the spectral-spatial pulse greatly aids in the visualization of these arteries. For the vessels we have studied so far, we have not found it necessary to provide muscle suppression. This may become necessary in the future, as we study smaller vessels and vessels that are surrounded by muscle instead of fat. If so, magnetization transfer contrast, late echoes, or inflow enhancement

could be used to suppress muscle. Also, these techniques may be necessary if the signal from the artery walls prevents adequate visualization of the lumen of the artery.

RESULTS

We used the fast spiral sequence of Fig. 2 to image the coronary arteries of normal volunteers and patients on a standard GE Signa 1.5-T whole-body imager. The images were acquired in 20-heartbeat breath-holds with 17.5-ms readout windows using a 13-cm receive-only surface coil positioned on the chest of the supine subjects. The surface coil was used for both FOV restriction and SNR enhancement. The static images were acquired during diastole by timing the acquisition to start either 335 ms after a plethysmograph trigger or at the *R* wave of an ecg waveform. The acquired resolution was $1.08 \text{ mm} \times 1.08 \text{ mm}$ (186×186 pixels over 20.0 cm). The flip angle was 90° for the static images and fat was suppressed using a spectral-spatial excitation pulse. The slice width varied between 3 and 10 mm. For some subjects, up to five overlapping slices were acquired on separate breath-holds to fully visualize a particular vessel.

Figure 4 shows two RAO images of the RCA of a normal volunteer. Approximately 8 cm of the RCA is visible in the two images. The slices were prescribed to be tangent to the heart in the axial scout scans. The 7-mm overlapping slices were acquired on successive excitations. Figure 5 shows an oblique axial, or Grüntzig, view of the left coronary artery of a normal volunteer. The left main coronary artery, the proximal circumflex, the LAD, and several branches of the LAD are visible. The slice was prescribed by the three-step procedure described in the previous section. The slice width was 5 mm.

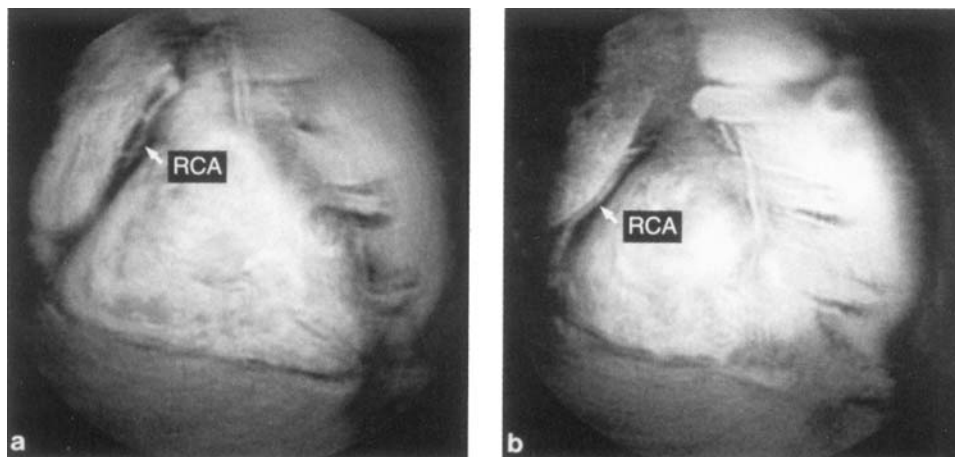


FIG. 4. Two right anterior oblique (RAO) images of the right coronary artery (RCA) of a normal volunteer. Approximately 8 cm of the RCA is visible. The slices were graphically prescribed from axial scout images. Each image was acquired during a single breath-hold (20 heartbeats, 17.5-ms readouts, 7-mm slices, 90° flip angle). Acquired resolution was $1.08 \text{ mm} \times 1.08 \text{ mm}$ (186×186 pixels over 20.0 cm). Displayed resolution is 256×256 pixels over 15.0 cm. The images were acquired 335 ms after a plethysmograph trigger. (a) Proximal segment. (b) Distal segment.

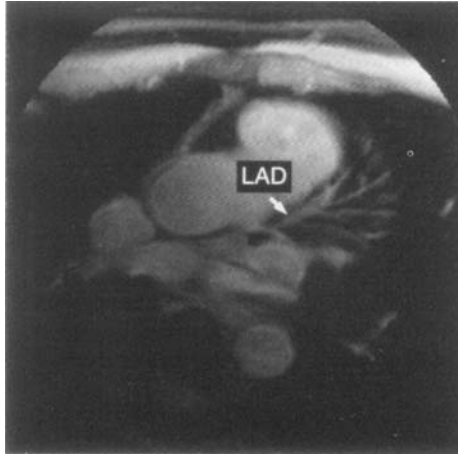


FIG. 5. Oblique axial (Grüntzig) view of the left coronary artery of a normal volunteer. The circumflex artery, left anterior descending coronary artery (LAD), and several diagonal branches of the LAD are visible. The slice was graphically prescribed from an RAO image of the LAD, which in turn was prescribed from an axial scout image. The slice width was 5 mm; all other parameters were the same as in Fig. 4.

Figure 6 shows a 3-mm axial slice of a patient with a known LAD lesion. The possible location of the lesion is shown by the arrow. The closest corresponding x-ray angiogram view to the MR image is shown in Fig. 7. The negative of this x-ray was flipped during developing to better match the view shown in the MR image, resulting

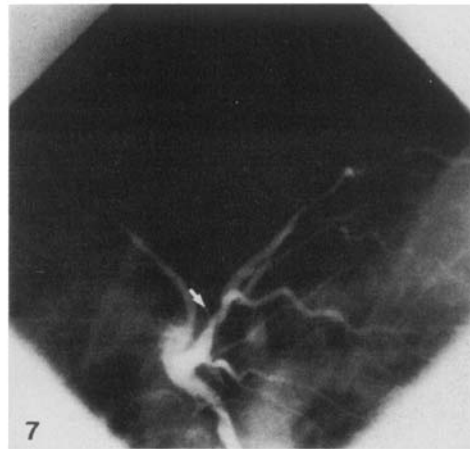
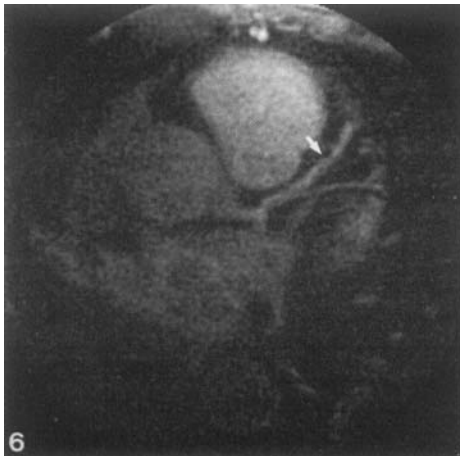


FIG. 6. Axial spiral image of a patient with a known LAD lesion. The possible location of the lesion is indicated by the arrow. The slice width was 3 mm; all other parameters were the same as in Fig. 4.

FIG. 7. Closest corresponding x-ray angiogram view to the image of Fig. 6. The location of the LAD lesion is indicated by the arrow. The overall coronary anatomy agrees with Fig. 6.

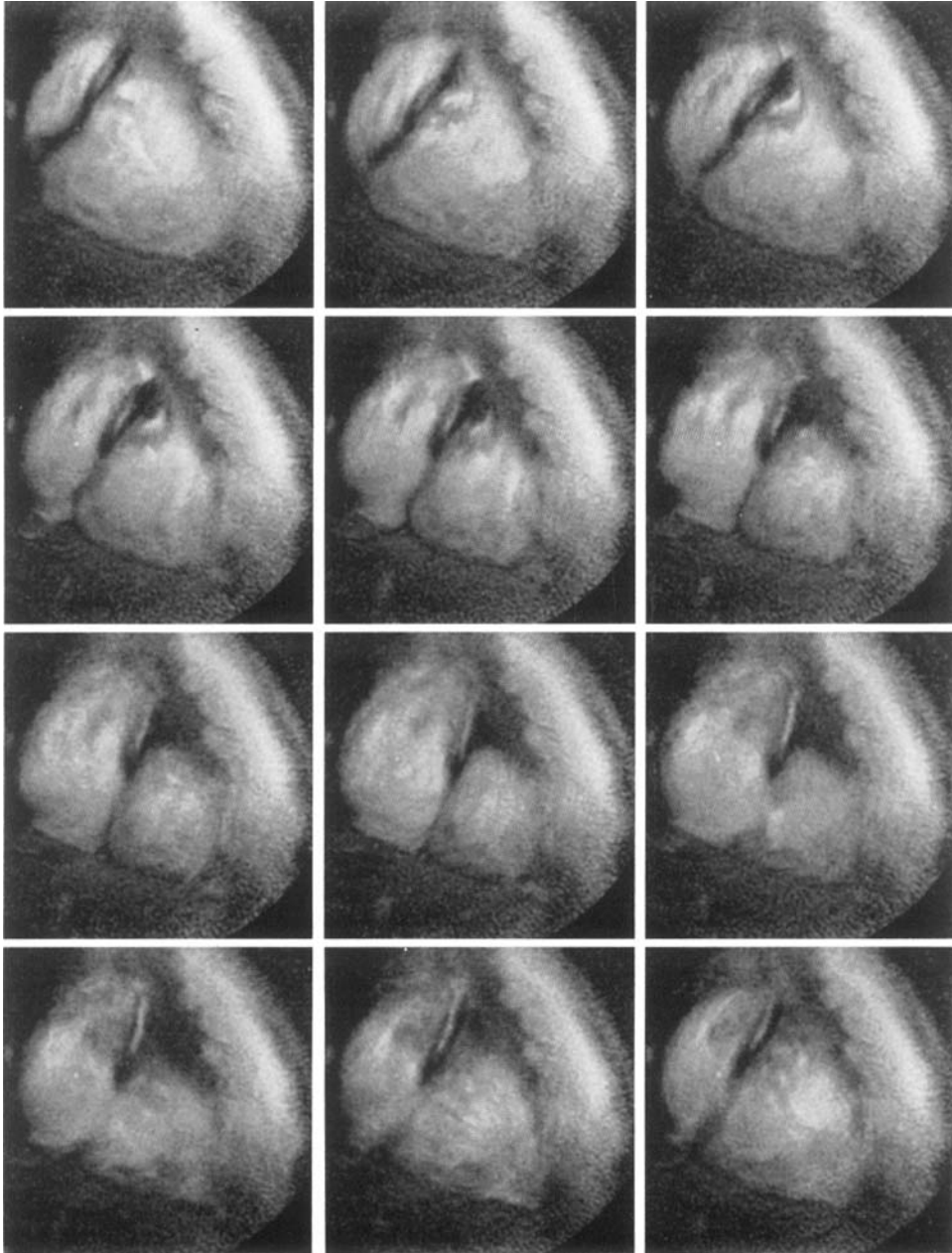


FIG. 8. Twelve-frame RAO movie of the RCA of a normal volunteer, acquired in a single breath-hold (7-mm slice, 45° flip angle). Various segments of the RCA come into view during the scan. The twelve temporal frames were acquired immediately after a plethysmograph trigger.

in a nonstandard x-ray view. The gross coronary anatomy is consistent between the MR and x-ray images; however, the lesion location is not conclusive in the MR image.

Figure 8 shows a 12-frame RAO movie of the RCA of a normal volunteer acquired during a single breath-hold. A 7-mm slice was used with a 45° flip angle. The TR was set to 50 ms to avoid saturation of the in-plane blood. While the SNR is lower than the static images, the movie presentation has the advantage of some suppression of the vessel wall and the surrounding muscle. It also is a fast way to view several different segments of the artery as they come into the slice. Note the large excursion of the RCA in these images. This indicates that any technique with an effective readout window longer than perhaps 25 ms might suffer from motion blurring.

DISCUSSION

Fast interleaved spiral imaging appears to be a robust method for breath-held coronary artery imaging. It offers SNR and temporal-resolution advantages over methods that use multiple excitations per heart cycle to collect multiple lines in *k* space. The fat suppression provided by a spectral-spatial pulse improves the visualization of the coronary arteries. The technique has proven to be a reliable way to image the coronary arteries of normal volunteers. Our experience with patients is in its early stages at this point, but the early results are encouraging.

In the future we plan to continue our patient studies. Patients tend to exhibit more anatomical variability than the healthy volunteers we have studied, so the localization procedure typically takes more time. We still must determine if lesions can be reliably seen with this technique, or whether further suppression of the vessel walls and muscle is necessary. We also must determine what role coronary movies should play in our protocols. One intriguing possibility for the future is to combine the movie technique with the injection of a paramagnetic contrast agent, thus combining high SNR, static tissue suppression, and temporal resolution. Lastly, we plan to combine spiral readouts with the selective inversion recovery technique, so that we can evaluate the relative merits of nonsubtractive and subtractive coronary artery imaging.

ACKNOWLEDGMENTS

The authors gratefully acknowledge the support from GE Medical Systems Group and the National Institutes of Health (Grants 1R01 HL39297 and 1R01 CA50948).

REFERENCES

1. S. J. WANG, B. S. HU, A. MACOVSKI, AND D. G. NISHIMURA, *Magn. Reson. Med.* **18**, 417 (1991).
2. D. BURSTEIN, *J. Magn. Reson. Imaging* **1**, 337 (1991).
3. R. R. EDELMAN, W. J. MANNING, D. BURSTEIN, AND S. PAULIN, *Radiology* **181**, 641 (1991).
4. C. L. DUMOULIN AND S. P. SOUZA, in "Proceedings, Ninth Annual Meeting of the Society of Magnetic Resonance in Medicine, 1990," p. 501.
5. Z. CHO, C. MUN, AND R. FRIEDENBERG, *Magn. Reson. Med.* **20**, 134 (1991).
6. C. B. PASCHAL, E. M. HAACKE, L. P. ADLER, W. LIN, A. SHETTY, AND R. J. ALFIDI, in "Proceedings, Ninth Annual Meeting of the Society of Magnetic Resonance in Medicine, 1990," p. 278.
7. S. PAULIN, G. K. VON SCHULTHESS, E. FOSSEL, AND H. P. KRAYENBUEHL, *AJR* **148**, 665 (1987).
8. K. M. LINK, in "SMRI Ninth Annual Meeting Program and Abstracts, 1991," Vol. 1, p. 171.
9. N. M. HYLTON, W. S. CHUNG, E. H. BOTVINICK, N. B. SCHILLER, P. SHELDON, AND L. KAUFMAN, *J. Digit. Imaging* **3**(1), 34 (1990).

10. A. MACOVSKI AND C. MEYER, in "Works in Progress, Fifth Annual Meeting of the Society of Magnetic Resonance in Medicine, 1986," p. 156.
11. C. H. MEYER AND A. MACOVSKI, *Magn. Reson. Imaging* **5**(6), 519 (1987).
12. C. H. MEYER AND A. MACOVSKI, in "Proceedings, Sixth Annual Meeting of the Society of Magnetic Resonance in Medicine, 1987," p. 230.
13. C. H. MEYER, A. MACOVSKI, AND D. G. NISHIMURA, in "Proceedings, Eighth Annual Meeting of the Society of Magnetic Resonance in Medicine, 1989," p. 362.
14. C. H. MEYER, A. MACOVSKI, AND D. G. NISHIMURA, in "Proceedings, Ninth Annual Meeting of the Society of Magnetic Resonance in Medicine, 1990," p. 403.
15. C. H. MEYER, J. M. PAULY, A. MACOVSKI, AND D. G. NISHIMURA, *Magn. Reson. Med.* **15** (1990).
16. P. MANSFIELD, *J. Phys. C* **10**, L55 (1977).
17. R. S. LIKES, U.S. Patent 4,307,343, 1981.
18. S. LJUNGGREN, *J. Magn. Reson.* **54**, 338 (1983).
19. C. B. AHN, J. H. KIM, AND Z. H. CHO, *IEEE Trans. Med. Imaging* **MI-5**(1), 2 (1986).
20. R. J. ORDIDGE, A. HOWSEMAN, R. COXON, R. TURNER, B. CHAPMAN, P. GLOVER, M. STEHLING, AND P. MANSFIELD, *Magn. Reson. Med.* **10**, 227 (1989).
21. R. R. RZEDZIAN AND I. L. PYKETT, *AJR* **149**, 245 (1987).
22. F. SCHMITT, M. STEHLING, R. LADEBECK, D. ATKINSON, AND M. FANG, in "Proceedings, Tenth Annual Meeting of the Society of Magnetic Resonance in Medicine, 1991," p. 841.
23. M. S. COHEN, R. W. WEISSKOFF, R. R. RZEDZIAN, AND H. L. KANTOR, *Magn. Reson. Med.* **14**(2), 409 (1990).
24. T. F. BUDINGER, H. FISCHER, D. HENTSCHEL, H.-E. REINFELDER, AND F. SCHMITT, *J. Comput. Assist. Tomogr.* **15**, 909 (1991).
25. C. H. MEYER, A. MACOVSKI, AND D. G. NISHIMURA, in "Proceedings, Ninth Annual Meeting of the Society of Magnetic Resonance in Medicine, 1990," p. 32.
26. J. M. PAULY, Ph.D. thesis, Stanford University, 1989.
27. C. HARDY AND H. CLINE, *J. Appl. Phys.* **66**, 1513 (1989).
28. J. L. DUERK AND O. P. SIMONETTI, *J. Magn. Reson. Imaging* **1**, 643 (1991).
29. R. WEISSKOFF, A. CRAWLEY, AND V. WEDEEN, in "Proceedings, Ninth Annual Meeting of the Society of Magnetic Resonance in Medicine, 1990," p. 398.
30. D. NISHIMURA, J. JACKSON, AND J. PAULY, *Magn. Reson. Med.* **22**(2), 481 (1991).
31. J. O'SULLIVAN, *IEEE Trans. Med. Imaging* **MI-4**, 200 (1985).
32. R. B. MARR, in "Works in Progress, Sixth Annual Meeting of the Society of Magnetic Resonance in Medicine, 1987," p. 25.
33. J. JACKSON, C. MEYER, D. NISHIMURA, AND A. MACOVSKI, *IEEE Trans. Med. Imaging* **10**, 473 (1991).
34. D. C. NOLL, C. H. MEYER, J. M. PAULY, D. G. NISHIMURA, AND A. MACOVSKI, *IEEE Trans. Med. Imaging* **10**, 629 (1991).
35. D. C. NOLL, J. M. PAULY, C. H. MEYER, D. G. NISHIMURA, AND A. MACOVSKI, *Magn. Reson. Med.* **25**(2), 319 (1992).